Additive Manufacturing Letters 6 (2023) 100155

Contents lists available at ScienceDirect

Additive Manufacturing Letters

journal homepage: www.elsevier.com/locate/addlet

Short Communication

3D characterization of magnetic phases through neutron polarization contrast tomography

Matteo Busi[a,*], Efthymios Polatidis[a], Stavros Samothrakitis[a], Patrick Köhnen[b], Florencia Malamud[a], Christian Haase[c], Markus Strobl[a,*]

[a] Laboratory for Neutron Scattering and Imaging, Paul Scherrer Institut, Villigen 5232, Switzerland
[b] GKN Additive, Pennefeldsweg 11-15, Bonn 53177, Germany
[c] Steel Institute, RWTH Aachen University, Intzestraße 1, Aachen 52072, Germany

A B S T R A C T

The advancement of laser-based metal additive manufacturing has enabled the production of near net shape complex geometries. Understanding the microstructural features of materials is crucial for accurate modeling of their mechanical behavior, particularly with regard to strain- or thermal-induced martensitic phase transformations in ferrous alloys and steels. For example, the formation of BCC α'-martensite can strengthen materials while preserving ductility of the dominating austenitic phase. However, in components where the shape memory effect is attributed to the reversible formation of ε-martensite, the accumulation of deformation-induced α'-martensite is an undesired, irreversible degradation mechanism. This study presents a novel tomographic approach utilizing polarization contrast neutron imaging for the 3D volumetric characterization of magnetic crystallographic phases, especially those present in low phase fractions that are typically undetectable with traditional techniques. The technique is applied to the study of strain-induced martensitic phase transformations in additively manufactured lattice structures made of high-Mn steels, which form small fractions of α'-martensite upon deformation. The results demonstrate the value of this technique for characterizing entire components and complex geometries found in numerous technological applications.

1. Introduction

Laser-based metal additive manufacturing (AM) is currently experiencing rapid growth due to its ability to produce lightweight components with complex shapes [1,2], as well as its potential to overcome limitations of traditional manufacturing methods [3]. The process involves various phase transformations of alloys, including solid-to-liquid and liquid-to-solid transformations during melting and solidification, as well as solid-state transformations during heating and cooling of the solidified material. Therefore, altering the transformation behavior is a powerful tool for controlling and customizing the microstructure formation during laser-based metal AM [4]. Accurately predicting and modeling the mechanical behavior of materials requires a deep understanding of these microstructural features, such as the interplay of phase transformations during thermal cycling or evolution of deformation-induced phase transformations during service. These properties are crucial for numerous engineering applications, including the automotive [5,6] and biomedical industries [7,8], civil applications [9], and their use as actuators [10,11]. One of the critical aspects of understanding microstructural properties is the characterization of strain- or thermal-induced martensitic phase transformations in ferrous alloys and steels. Here one needs to distinguish between ε-martensite with hexagonal close-packed (HCP) crystal structure and α'-martensite with body centered cubic (BCC) crystal structure. In general, ε-martensite forms in low stacking fault energy (SFE) materials like ferrous shape memory alloys (SMA) [12] and high-Mn steels [13], where small quantities of α'-martensite can also be traced [14,15]. In higher SFE steels like 304L [16] or 20,117 stainless steels, α'-martensite can form from intermediate ε-martensite or directly from austenite. Moreover, in low SFE steels, ε-martensite is a precursor for the formation of α'-martensite [17]. The formation of BCC α'-martensite plays a vital role in strengthening the material, while still preserving its ductility, owing to the presence of large amount of austenite, achieving an ideal equilibrium between these two properties. Nevertheless, when it comes to components made from e.g. ferrous SMAs, where the shape memory effect is attributed to the reversible formation of ε-martensite, the accumulation of deformation-induced α'-martensite is an undesired, irreversible degradation mechanism [15] that necessitates focused analysis. The development of robust and experimentally verified computational tools is essential to accelerate the development and utilization of advanced manufacturing and materials. To achieve this goal, continued progress in characterizing microstructural properties and understanding the mechanisms of phase transformations is critical.

Conventional microstructural characterization techniques, such as optical microscopy, electron microscopy, electron backscatter diffraction (EBSD) and X-ray diffraction, are often limited to surface observations or small-sized material samples, making them insufficient for providing a representative picture of the bulk. Furthermore, destructive approaches are often necessary for access to the bulk, hindering in-situ ob-

* Corresponding authors.
E-mail addresses: matteo.busi@psi.ch (M. Busi), markus.strobl@psi.ch (M. Strobl).

https://doi.org/10.1016/j.addlet.2023.100155
Received 3 May 2023; Received in revised form 29 May 2023; Accepted 31 May 2023

servations of phase evolution. While advanced synchrotron X-ray techniques, such as 3D-XRD [18] and X-ray diffraction contrast tomography [19], can provide unique insights through 3D microstructure maps, their application is typically limited to small sample volumes with rather simple shapes. Additionally, the degree of mosaicity can be a limiting factor when studying plastically deformed materials. Neutrons offer a unique approach for bulk microstructure characterization. However, obtaining spatially resolved insights into meso-scale phenomena in polycrystalline materials' bulk requires the development of novel neutron imaging methods. Wavelength-resolved diffraction contrast neutron imaging has been utilized extensively for 2- and 3-dimensionally mapping phase distributions [20–26] and observing phase evolution [27–29], with spatial resolutions down to a few tens of micrometers. However, to achieve high resolution and identify small fractions and subtle phase changes, exposure times up to several hours are often necessary depending on the specific instrumental setup used. Recently, we have presented a novel imaging method for the spatially resolved mapping of magnetic crystallographic phases [30], based on polarization contrast neutron imaging (PNI) [31,32]. This method is only sensitive to the presence of non-parallel magnetic field components with respect to the initial polarization and is thus not affected by other crystallographic features such as e.g. texture, grain size, mosaicity. In particular, thanks to its short exposure time required, this method is very efficient for time-resolved observations of phase evolution during e.g. in-situ load tests, heat treatment or laser processing. Furthermore, its high sensitivity to small magnetic phase fractions makes it a strong alternative, especially when traditional neutron techniques prove insufficient (e.g. neutron diffraction, Bragg edge imaging). However, the study was limited to relatively simple sample geometries, for which a radiographic 2D mode serves well enough. Here we present a multimodal tomographic approach utilizing PNI, which is able to provide 3D volumetric maps of martensitic phase fractions, in addition and complementary to the conventional attenuation contrast maps, which is efficient in particular for investigations of samples with complex shapes such as lattice structures. The method is applied to the study of strain-induced martensitic phase transformations in additively manufactured lattice structures made of high-Mn steels that have been seen to form small fractions of α'-martensite upon deformation [33].

2. Material and methods

2.1. Instrumentation and method

The measurements were conducted at the BOA beamline [34] of the Paul Scherrer Institut's Swiss spallation neutron source. The beam projected by the imaging pinhole at BOA is naturally polarized, with the neutron spin state oriented in a specific vertical direction, thanks to the polarizing bender unit permanently installed upstream the pinhole. The PNI instrumentation setup includes an adiabatic fast spin flipper, which can interactively induce a π shift in the neutron beam's polarization vector. A magnetic guide field of approximately 0.52 T is present throughout the neutron beam to maintain its polarization. Adjacent and upstream of the imaging detector, a neutron spin filter with an active field of view of 4×4 cm^2 is installed to allow analysis of the beam's spin state and, thus, polarization (and depolarization). To convert captured neutrons into light, a 100 μm thick Li/ZnS:Ag scintillator screen measuring 16×16 cm^2 was used. The light is then reflected by a mirror and detected using the Andor iKon-M CCD camera equipped with a 1024×1024 pixels readout chip. A magnification lens was mounted on the camera and configured to provide an active field of view of 67.5×67.5 mm^2, resulting in an effective pixel size of 66 μm.

A PNI radiograph (or projection, when using computed tomography) involves acquiring a pair of images corresponding to opposite neutron spin states (e.g., spin-up $I_\uparrow$ and spin-down $I_\downarrow$) obtained by operating the spin flipper. These two images are then summed to obtain the total beam intensity ($I = I_\uparrow + I_\downarrow$), while the beam polarization is calculated as the ratio of their difference to their sum ($P = \frac{I_\uparrow - I_\downarrow}{I_\uparrow + I_\downarrow}$). To calculate transmission and depolarization, the sample acquisitions (I) are normalized to reference open beam acquisitions (I_0), and these values are used to derive attenuation ($\mu = \log(I/I_0)/t$) and depolarization coefficient ($\eta = \log(P/P_0)/t$), where t is the sample thickness. In the tomographic approach introduced in this work, multiple PNI projections are acquired as the sample is rotated around a vertical axis. These normalized transmission and depolarization sinograms are then reconstructed using computer algorithms to create attenuation and depolarization contrast voxelized volumes. The volumetric reconstruction procedure automatically carries out thickness correction accurately when the pixel size is well-determined. The attenuation coefficient provides a volumetric mapping that is linearly dependent on the bulk density of a specimen, making it useful for detecting structural defects such as cracks and porosity. On the other hand, the depolarization coefficient provides a volumetric mapping that is linearly dependent on the amount of magnetic phases present. By calibrating with reference samples of known phase fractions, it is possible to quantitatively determine the magnetic phase fraction in a sample. Since the beam geometry is identical for both modes, the resulting attenuation and depolarization contrast voxelized volumes are naturally registered, eliminating the need for further image alignment procedures. This allows for the spatially-dependent information about bulk density and martensitic phase fraction to be correlated without additional steps.

The samples dimension allowed two specimens to be placed simultaneously on a rotation stage within the field of view of the spin analyzer for each tomographic scan. A total of 232 projections were taken over a full 360° rotation with a step size of approximately 1.55° per projection angle. Each projection angle was imaged twice, for spin-up and spin-down configurations respectively, with a total exposure time of 300 s. Including the open beam acquisition for normalization, each tomography took approximately 19 h to complete. The tomographic reconstructions were performed using the ASTRA [35] open source software, utilizing the SIRT [36] algorithm for reconstruction and pre-processing algorithms for correcting spot and ring artifacts. Finally, the reconstructed volumes were subjected to a total variation regularization denoising [37] to enhance overall image quality.

2.2. Materials and experiments

Lattice structures with a geometry similar to those presented by Köhnen et al. [33] were manufactured from X30Mn21 steel powder (see chemical composition and CAD geometry of the lattice structure in Ref. [33], provided by Thyssenkrupp Raw Materials GmbH in Germany. Each unit cell of the lattice structure has an edge length of 3 mm and a strut diameter of 500 μm. The X30Mn21 powder was atomized using the electrode induction melting gas atomization technique with argon gas. The laser powder bed fusion (LPBF) process was carried out using an EOS SINT 270 LPBF machine (EOS GmbH, Germany) equipped with a single-mode fiber Yb:YAG-laser with a Gaussian intensity profile (focus diameter of 80 μm). The laser power was set to 120 W. Furtherore, a scan speed of 750 mm/s, hatch spacing of 70 μm and layer thickness of 30 μm were used. The samples were produced under an Ar atmosphere with a purity level of ≥ 99.996% and a flow rate of 3 L/min, which resulted in an excess pressure of 100 mbar in the build chamber and an average O2 concentration of about 100 ppm. The laser scan strategy involved bidirectional scanning and alternating 33° rotations at each layer. Four lattice structure samples with identical geometry were produced for the experiments. One sample was left in its virgin state, while the other three were subjected to compression loads ex-situ to examine the formation of α'-martensite phase fractions at various compression levels. The compression load was applied using a servo-hydraulic universal testing machine (Carl Shenk AG, Germany) equipped with a 400 kN load cell and was conducted at room temperature. The three samples underwent compression at fixed strain rate of 0.001/s until reaching 10%, 20% and

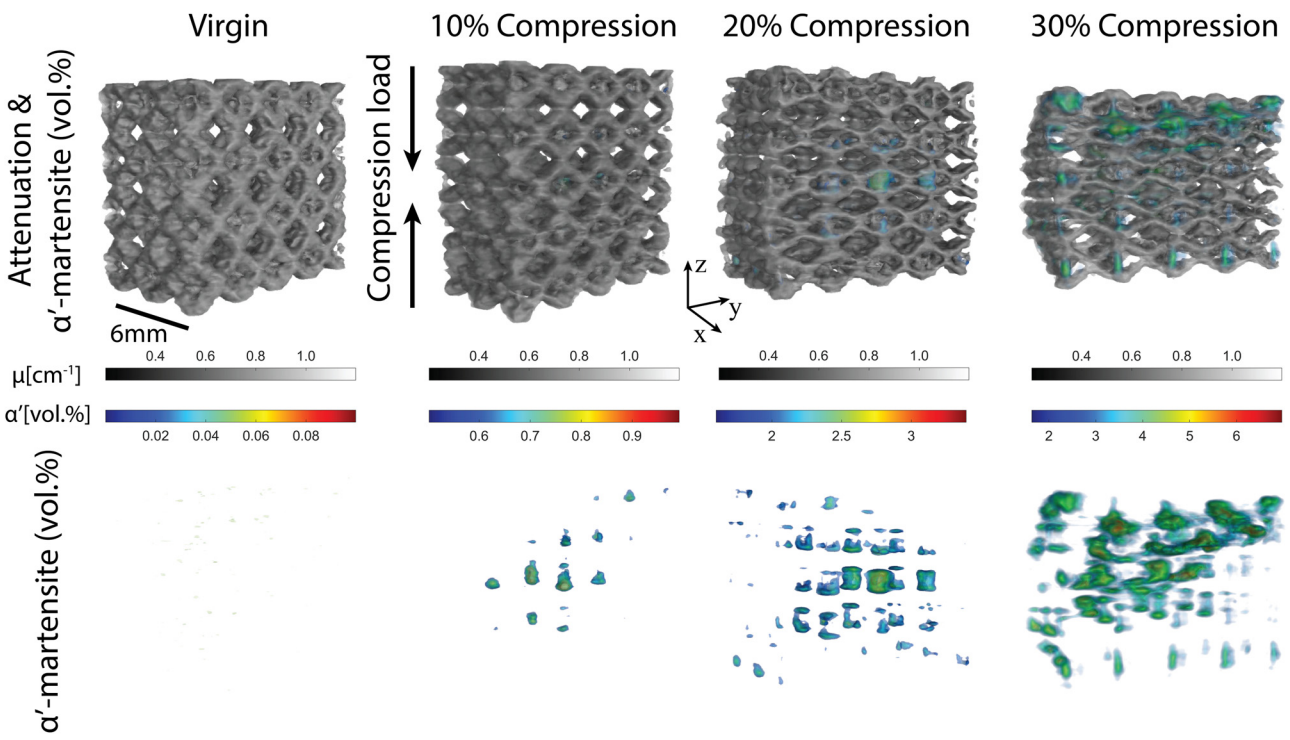

Fig. 1. Volumetric reconstructions of the samples in their virgin state and after undergoing relative compression loads of 10%, 20%, and 30%. The top row shows overlapped volumetric maps of linear attenuation coefficient (cm^{-1}) and α'-martensite phase fraction (vol.%), while the bottom row displays only the α'-martensite phase fraction. The compression load direction and scale bar are indicated and valid for all samples.

30% compression with respect to their initial height. The virgin sample had a repeated unit cell geometry of $2 \times 4 \times 4$ with respect to the Cartesian axes shown in Fig. 1, resulting in a volume of $6 \times 12 \times 12$ mm^3. The compressed samples, on the other hand, were produced with an initial repeated unit cell geometry of $2 \times 4 \times 5$, meaning that they had one additional cell layer in the compression load direction.

3. Results and discussion

Fig. 1 presents volumetric reconstructions of the four samples measured using PNI tomography. To visualize where in the sample the α'-martensite is located we show the overlap between attenuation contrast, which is proportional to bulk density, and α'-martensite phase fraction volume maps. Additionally, the isolated volume maps of the α'-martensite phase fraction are also shown. In order to enhance the visibility of color gradients within each sample, the color scale relative to the α'-martensite phase fraction varies for each sample. This variation is necessary because the distribution of phase fraction is heavily skewed toward higher values with increasing sample compression. The results of the study show a direct correlation between the sample compression and the resulting α'-martensite phase fraction. Specifically, the mean α'-martensite phase fraction throughout the entire sample volume increases from 0.01% under virgin conditions (where contributions are likely due to statistical noise) to 0.04%, 0.21%, and 0.44% for compression strains of 10%, 20%, and 30%, respectively. It is worth noting that the mean value is relatively low due to the inclusion of parts of the sample that do not transform. Furthermore, the maximum α'-martensite phase fraction obtained in the samples corresponds to 1.33%, 4.50%, and 9.41% for 10%, 20%, and 30% compression of the lattice, respectively.

In order to fully understand the transformation of the samples under different compression loads, histograms of the volume fraction versus the phase fraction of α'-martensite were calculated and extracted from the reconstructions. Fig. 2a) displays the histograms obtained for the four samples. This graph provides valuable insight into how the distribution of phase fractions within the sample volume evolves with increasing compression. It reveals that the distribution of phase fraction broadens overall with increasing compression, and higher phase fractions are observed in regions where the sample is most deformed. Conversely, the virgin sample exhibits a phase fraction distribution centered on values close to zero, with any deviations from zero being attributed to statistical noise resulting from the tomographic reconstruction or the presence of small fractions of iron oxides, which are ferromagnetic, in the material.

To provide further insight into the correlation between lattice structure compactness due to deformation and the resulting martensitic transformation, a bivariate histogram of α'-martensite versus the binarized material density was calculated for each sample. To obtain the binarized material density, a binary thresholding mask was applied to the attenuation contrast volume maps. In this mask, zero values represent the absence of material in the voxel, while unity values represent the presence of material in the voxel. Next, a moving average with a convolution kernel size of $20 \times 20 \times 20$ voxels was applied to the mask, resulting in a 3D matrix of the same size as the original volumetric reconstruction. The values in this matrix represent the average presence of materials within a 20-voxel window in each direction, hence binarized material density. Isolated lattice strut voxels have smaller binarized material density than voxels at the intersection between lattice struts. Similarly, voxels where the lattice structure has been compressed and has become more compact have greater values than respective undeformed voxels or struts that have expanded due to tensile stresses. Overall, an increase in α'-martensite phase fraction is observed with increasing compression loads, as well as an increase in the binarized material density distribution due to the lattice structure becoming more compact upon compression. Notably, the highest α'-martensite phase fractions are found at the highest binarized material densities in the samples that underwent 20% and 30% compression of the lattice, highlighting the correlation between deformation amplitude and the martensitic transformation.

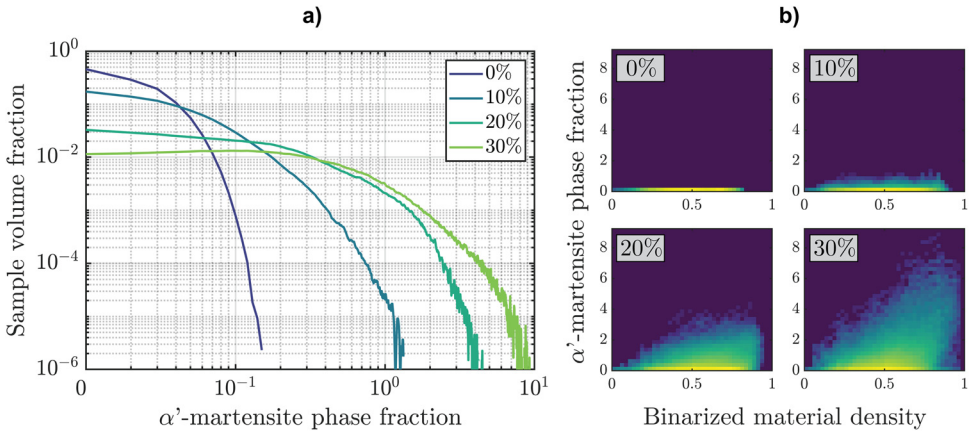

Fig. 2. (a) Histograms depicting the distribution of α'-martensite phase fractions (vol.%) in the four measured samples, plotted against their corresponding sample volume fraction (vol.%). (b) Bivariate histograms displaying the correlation between α'-martensite phase fraction and binarized material density for each sample.

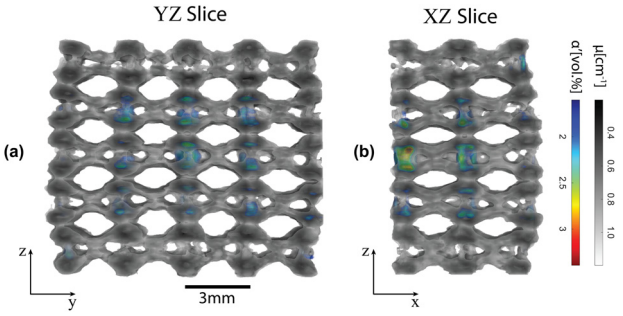

Fig. 3. (a) YZ-plane and (b) XZ-plane slices of the sample undergone a 20% compression of the lattice. The overlapped volumetric maps show the linear attenuation coefficient (cm^{-1}) and α'-martensite phase fraction (vol.%), with the same color bar shown on the right-hand side applying to both slices.

Fig. 3 presents selected orthogonal YZ-plane and XZ-plane slices of the sample that underwent a 20% compression of the lattice. It can be observed that the lattice struts toward the center of the volume undergo shrinkage upon compressive deformation, resulting in martensitic transformation, particularly at the intersections between the struts, where the highest local strain during compression was observed by digital image correlation analysis [38]. Furthermore it was shown by Köhnen et al. [33], using destructive EBSD analysis of comparable samples, that the strut intersections undergo almost complete transformation to ε-martensite during plastic deformation. We note that the presented method is exclusively sensitive to α'-martensite, which is ferromagnetic and it is anticipated to form from previously formed ε-martensite. However, the low phase fraction and typically small size of α'-martensite particles, is challenging to be detected and quantified using microscopy methods, e.g. with EBSD. As a result, the overall lattice structure expands horizontally, perpendicular to the compression load direction, due to the rearrangement of the lattice struts. The lattice struts towards the external sides of the sample also undergo martensitic transformation, possibly due to tensile stresses induced by the rearrangement of the structure. In contrast, the XZ-plane slice exhibits a preferential compression, potentially due to shear forces, in the leftmost section of the sample, where the highest martensitic transformation occurs. In the middle section of the sample, both martensitic transformation, to a lesser degree at the central strut intersections, and deformation with respect to the vertical axis due to tensile stresses are observed. The latter deformation is also seen to a greater extent in the rightmost section of the sample, where the sample seems to expand horizontally. It is worth noting that the cross-shaped struts connecting the lattice structure are the least prone to martensitic transformation.

It can be speculated that during additive manufacturing of the lattice structures the homogeneous concentration of Mn in the material is not preserved, due to Mn evaporation being potentially different in different regions of the heterogeneous sample structures. Due to the fact that Mn is an austenite stabiliser, this could affect stronger martensitic transformation in some regions. While no direct correlation can be established based on the presented study, this might indeed be a route of future research utilizing this method.

4. Conclusions

The present study demonstrates the successful application of polarization contrast neutron tomography for the 3D mapping of α'-martensite phase fractions in iron-based additively manufactured lattice structure specimens subjected to varying relative compression strains. The technique offers a multimodal approach, which allows for correlating the sample deformation observed in the attenuation contrast volumes with the yielded martensitic transformation observed through the neutron beam depolarization induced by ferromagnetic phases in the material. Our study revealed a direct correlation between the compressive deformation, in particular at the strut intersections of the lattice structure, and the formation of α'-martensite, consistent with previous research that used digital correlation image analysis to reveal local strains. Additionally, we observed that the cross-shaped struts connecting the lattice structure, where the smallest compressive strains were found, were the least affected by martensitic transformation. The exceptional sensitivity of the method to low martensitic phase fractions makes it a robust alternative to conventional techniques like e.g. neutron diffraction, which struggles to reliably detect such low phase fractions. Moreover, the volumetric spatial resolution provided by the tomographic approach enables efficient evaluation of the full scale distribution in bulk samples with complex geometry morphologies like the lattice structure specimens examined in this study. Furthermore, the technique can complement or validate results obtained through finite element analysis simulations, or contribute to improving the accuracy of physical models integrated in simulation frameworks. Although the presented tomographies were carried out over a relatively long period of time, it is important to note that the method only requires exposure times of a few tens of seconds per projection. This makes it possible to conduct in-situ deformation tests at multiple intermediate compression steps and perform fast tomography at a much higher time rate. In summary, polarization contrast neutron tomography is a promising and effective tool for studying the ferromagnetic phase transformation in iron-based materials and has potential applications in a wide range of additively manufactured materials.

Declaration of Competing Interest

The authors declare that they have no known competing financial interests or personal relationships that could have appeared to influence the work reported in this paper.

Data availability

Data will be made available on request.

Acknowledgments

The authors acknowledge allocation of in-house beamtime at the BOA beamline at Paul Scherrer Institut (Switzerland). CH would also like to acknowledge the support of the German Federal Ministry of Education and Research within the NanoMatFutur project “MatAM - Design of additively manufactured high-performance alloys for automotive applications” (project ID 03XP0264).

References

[1] K.V. Wong, A. Hernandez, A review of additive manufacturing, Int. Sch. Res. Not. 2012 (2012) 208760, doi:10.5402/2012/208760.
[2] C. Druzgalski, et al., Process optimization of complex geometries using feed forward control for laser powder bed fusion additive manufacturing, Addit. Manuf. 34 (2020) 101169.
[3] T. Pereira, J.V. Kennedy, J. Potgieter, A comparison of traditional manufacturing vs additive manufacturing, the best method for the job, Procedia Manuf. 30 (2019) 11–18.
[4] C. Sofras, et al., Tailored deformation behavior of 304L stainless steel through control of the crystallographic texture with laser-powder bed fusion, Mater. Des. 219 (2022) 110789.
[5] S.G. Sarvankar, S.N. Yewale, Additive manufacturing in automobile industry, Int. J. Res. Aeronaut. Mech. Eng 7 (2019) 1–10.
[6] J.C. Vasco, Additive manufacturing for the automotive industry, in: Additive Manufacturing, Elsevier, 2021, pp. 505–530.
[7] M. Vignesh, et al., Development of biomedical implants through additive manufacturing: a review, J. Mater. Eng. Perform. 30 (2021) 4735–4744.
[8] R. Allavikutty, P. Gupta, T.S. Santra, J. Rengaswamy, Additive manufacturing of Mg alloys for biomedical applications: current status and challenges, Curr. Opin. Biomed. Eng. 18 (2021) 100276.
[9] K. Jamali, V. Kaushal, M. Najafi, Evolution of additive manufacturing in civil infrastructure systems: a ten-year review, Infrastructures 6 (2021) 108.
[10] O. Fogel, et al., 3D printing of functional metallic microstructures and its implementation in electrothermal actuators, Addit. Manuf. 21 (2018) 307–311.
[11] H.K. Jayant, M. Arora, Droplet-on-demand metal additive manufacturing using a magnetostrictive actuator, J. Manuf. Process. 83 (2022) 86–96.
[12] A. Arabi-Hashemi, E. Polatidis, M. Smid, T. Panzner, C. Leinenbach, Grain orientation dependence of the forward and reverse fcc hcp transformation in femnsi-based shape memory alloys studied by *in situ* neutron diffraction, Mater. Sci. Eng. A 782 (2020) 139261.
[13] Y.S. Chun, J.S. Kim, K.T. Park, Y.K. Lee, C.S Lee, Role of ε martensite in tensile properties and hydrogen degradation of high-Mn steels, Mater. Sci. Eng. A 533 (2012) 87–95.
[14] C. Haase, et al., Exploiting process-related advantages of selective laser melting for the production of high-manganese steel, Materials 10 (2017) 56 Basel.
[15] I. Ferretto, et al., Shape memory and mechanical properties of a Fe-Mn-Si-based shape memory alloy: effect of crystallographic texture inherited by additive manufacturing, Mater. Des 229 (2023) 111928.
[16] A.K. De, D.C. Murdock, M.C. Mataya, J.G. Speer, D.K. Matlock, Quantitative measurement of deformation-induced martensite in 304 stainless steel by X-ray diffraction, Scr. Mater. 50 (2004) 1445–1449.
[17] E. Polatidis, et al., Suppressed martensitic transformation under biaxial loading in low stacking fault energy metastable austenitic steels, Scr. Mater. 147 (2018) 27–32.
[18] H.F. Poulsen, Three-dimensional X-ray Diffraction microscopy: Mapping Polycrystals and Their Dynamics, 205, Springer Science & Business Media, 2004.
[19] A. King, G. Johnson, D. Engelberg, W. Ludwig, J. Marrow, Observations of intergranular stress corrosion cracking in a grain-mapped polycrystal, Science 321 (2008) 382–385.
[20] R. Woracek, et al., 3D mapping of crystallographic phase distribution using energy-selective neutron tomography, Adv. Mater. 26 (2014) 4069–4073.
[21] H. Sato, et al., Relation between Vickers hardness and Bragg-edge broadening in quenched steel rods observed by pulsed neutron transmission imaging, Mater. Trans. 56 (2015) 1147–1152.
[22] M.G. Makowska, et al., Investigating phase behavior and structural changes in NiO/Ni-YSZ composite with monochromatic in-situ 2D and static 3D neutron imaging, Phys. B Condens. Matter 551 (2018) 24–28.
[23] W. Woo, et al., Multi-scale analyses of constituent phases in a trip-assisted duplex stainless steel by electron backscatter diffraction, *in situ* neutron diffraction, and energy selective neutron imaging, Scr. Mater. 158 (2019) 105–109.
[24] E. Polatidis, et al., Neutron diffraction and diffraction contrast imaging for mapping the trip effect under load path change, Materials 13 (2020) 1450 Basel.
[25] M. Bacak, et al., Neutron dark-field imaging applied to porosity and deformation-induced phase transitions in additively manufactured steels, Mater. Des. 195 (2020) 109009.
[26] M. Busi, et al., Frame overlap Bragg edge imaging, Sci. Rep. 10 (2020) 1–10.
[27] M.G. Makowska, et al., *In situ* time-of-flight neutron imaging of NiO–YSZ anode support reduction under influence of stress, J. Appl. Crystallogr. 49 (2016) 1674–1681.
[28] M.G. Makowska, et al., Coupling between creep and redox behavior in nickel-yttria stabilized zirconia observed in-situ by monochromatic neutron imaging, J. Power Sources 340 (2017) 167–175.
[29] E. Dabah, et al., Time-resolved Bragg-edge neutron radiography for observing martensitic phase transformation from austenitized super martensitic steel, J. Mater. Sci. 52 (2017) 3490–3496.
[30] M. Busi, et al., Polarization contrast neutron imaging of magnetic crystallographic phases, Mater. Today Adv. 16 (2022) 100302.
[31] N. Kardjilov, I. Manke, R. Woracek, A. Hilger, J. Banhart, Advances in neutron imaging, Mater. Today 21 (2018) 652–672.
[32] M. Strobl, et al., Polarization measurements in neutron imaging, J. Phys. D Appl. Phys. 52 (2019) 123001.
[33] P. Köhnen, S. Ewald, J.H. Schleifenbaum, A. Belyakov, C. Haase, Controlling microstructure and mechanical properties of additively manufactured high-strength steels by tailored solidification, Addit. Manuf. 35 (2020) 101389.
[34] M. Morgano, S. Peetermans, E. Lehmann, T. Panzner, U. Filges, Neutron imaging options at the BOA beamline at Paul Scherrer Institut, Nucl. Instrum. Methods Phys. Res. Sect. A Accel. Spectrometers Detect. Assoc. Equip. 754 (2014) 46–56.
[35] W. Van Aarle, et al., Fast and flexible X-ray tomography using the ASTRA toolbox, Opt. Express 24 (2016) 25129–25147.
[36] W.J. Palenstijn, J. Bédorf, K.J. Batenburg, A distributed SIRT implementation for the ASTRA toolbox, in: Proceedings of the Fully Three-Dimensional Image Reconstruction Radiology Nuclear Medicine, 2015, pp. 166–169.
[37] A. Chambolle, V. Caselles, D. Cremers, M. Novaga, T. Pock, An introduction to total variation for image analysis, Theory Found. Numer. Methods Sparse Recovery 9 (2010) 227.
[38] P. Köhnen, et al., Mechanical properties and deformation behavior of additively manufactured lattice structures of stainless steel, Mater. Des. 145 (2018) 205–217.